INVESTIGATING TSUNAMI-IONOSPHERIC COUPLING EFFICIENCY

BY

MATTHEW A. GRAWE

Senior Thesis in Electrical Engineering

University of Illinois at Urbana-Champaign

Advisor: Jonathan J. Makela

May 2015

ABSTRACT

Coupling has been shown to exist between tsunamis and the upper atmosphere, making their detection in the total electron content (TEC) and the airglow layer possible. However, a quantitative relationship between the strength of the ionospheric signature and the sea level variation remains elusive. Here, we show the ionospheric detection of the 28 October 2012 Haida Gwaii tsunami in both the TEC and the airglow layer. Previously reported ionospheric signatures from the 11 March 2011 Tohoku tsunami are re-explored in comparison to the newer Haida Gwaii detections. Both events provide excellent test cases in the study of tsunami ionospheric coupling efficiency, which is most notably affected by the observation geometry and the tsunami propagation direction. A simple a priori model based on the problem geometry is developed that predicts the relative coupling efficiency while also incorporating the observability of the gravity wave. Predictions are compared to observations and the limitations of the model are discussed in an effort to motivate future studies.

Keywords: ionosphere, tsunami, airglow, total electron content, GPS, magnetic field

To my parents, for their love and support

ACKNOWLEDGMENTS

Work on this research at the University of Illinois at Urbana-Champaign was supported by the Office of Naval Research grant N00014-13-1-0350.

TABLE OF CONTENTS

CHAPTER 1

INTRODUCTION

Tsunamis are known to couple into the atmosphere by generating internal gravity waves that travel to ionospheric heights. The initial theory regarding atmospheric gravity waves was developed by *Hines* (1960), followed by the analysis of *Hooke* (1968) in describing the response of electron and ion densities in the ionosphere perturbed by atmospheric gravity waves. *Peltier and Hines* (1976) approached the problem directly, ultimately predicting that sea surface variations typical of tsunamis can seed internal gravity waves with amplitudes strong enough for ionospheric detection.

Artru et al. (2005) presented the first observations of a tsunami's signature in the ionospheric total electron content (TEC) using the dense Japanese GPS Earth Observation Network (GEONET) for the tsunami generated by the 23 June 2001 earthquake in Peru. The TEC detection technique has gained considerably more attention in the years following, with observations of the 26 December 2004 Indian Ocean tsunami by *Liu et al.* [2006a, 2006b] and several detections from other tsunamis by *Lognonné et al.* (2006). *Occhipinti et al.* (2006) achieved a significant step forward with the numerical reproduction of the TEC signatures from the 2004 Sumatra tsunami. *Occhipinti et al.* (2008) explored the dependence of the observation on geomagnetic latitude. Three more earthquake and tsunami events (15 November 2006 at Kuril Islands, 29 September 2009 at Samoa Islands, and 27 February 27 2010 at Chile) produced variation in the TEC, shown by *Rolland et al.* (2010) for GPS networks distant from the epicenter.

Other observing modalities and models have been shown to be effective at studying the effects of the tsunami-generated gravity waves in the ionosphere. For example, *Makela et al.* (2011) presented the first detection of tsunami-ionospheric coupling via airglow imaging for the 11 March 2011 tsunami generated by the Tohoku earthquake. The airglow signature had been previously hypothesized by *Hickey et al.* (2010), but had never before been observed.

Occhipinti et al. (2013) explored the detection of ionospheric signatures in the TEC generated both by the source rupture and the tsunami close to the epicenter, where the signal can consist not only of the internal gravity wave component, but also acoustic and Rayleigh wave-induced fluctuations.

Despite the recent increase in the number of detections, work remains before an understanding of the relationship between the geometrical characteristics of the tsunami, atmospheric gravity wave, and ionospheric signature will become clear enough to accurately relate sea surface variation directly to the ionospheric response, or vice versa. The strong TEC signatures we present caused by the 28 October 2012 Haida Gwaii event (larger than those seen during the passage of the stronger Tohoku tsunami) indicate that tsunami-ionospheric coupling efficiency does not simply scale with the height of the tsunami wave. We develop and utilize a model to investigate why the TEC signatures for the Haida Gwaii event were larger than those seen during the passage of the stronger Tohoku tsunami. The work of *Hooke* (1968) (especially on the importance of considering the relative orientation between the gravity wave and the geomagnetic field) underlies a key portion of the model. Additionally, we show another detection in the airglow layer using an imaging system from the same location used by *Makela et al.* (2011).

In this thesis, techniques for extracting ionospheric signatures induced by tsunamis are presented and then utilized in two case studies. It should be noted that some, but not all, of the content in this work is being prepared for journal publication. Chapter 2 discusses the specifics of the TEC and airglow techniques used to quantify ionospheric perturbations and infer gravity wave parameters. Chapter 3 discusses the efficiency of the coupling between a tsunami and the ionospheric signature, most importantly the consideration of tsunami propagation direction and observation geometry. Chapter 4 takes an in-depth look at the 28 October 2012 Haida Gwaii and 11 March 2011 Tohoku tsunamis, their associated ionospheric signals, and the efficiency at which both tsunamis couple into the ionosphere using the knowledge from the previous chapters. Finally, Chapter 5 presents a comparison of the case studies where some important conclusions about observability conditions are hypothesized and used to motivate future study.

CHAPTER 2

MEASUREMENT TECHNIQUES

2.1 Total Electron Content

The total electron content (TEC) is an integrated measurement that represents the total number of electrons along the integration path (typically taken between a satellite and receiver). The dispersive nature of the ionosphere causes the satellite-receiver signal propagation time to vary with frequency in addition to being a function of the total number of electrons between the satellite and receiver. The difference between two frequency-dependent delays is measurable with a dual-frequency GPS receiver using two different methods: one using pseudoranges (P) and the other using phase ranges (L). Most publicly available, dense, dual-frequency GPS networks make both quantities available. The two frequencies used are the GPS L_1 and L_2 frequencies, taking the values $f_{L1} = 1575.42$ MHz and $f_{L2} = 1227.60$ MHz, respectively. From *Makela* (2003), the differential delay $\Delta(\delta t)$ between the L1 and L2 signals is equal to

$$\Delta(\delta t) = 40.3 \frac{TEC}{c} \frac{f_{L1}^2 - f_{L2}^2}{f_{L1}^2 f_{L2}^2} \tag{2.1}$$

where c is the speed of light. The difference between the pseudoranges is

$$\Delta P = P_{L1} - P_{L2} \tag{2.2}$$

which is proportional to the differential delay (since $P = c\,\delta t$):

$$\Delta(\delta t) = \frac{\Delta P}{c}$$

which lets us obtain the TEC as

$$TEC = \frac{\Delta P}{40.3} \frac{f_{L1}^2 f_{L2}^2}{f_{L1}^2 - f_{L2}^2} + mp + B \tag{2.3}$$

with mp representing multipath noise and B representing satellite and receiver clock biases.

Alternatively, TEC can be derived using measurements of phase range. Typically, cycle counts are reported by a GPS network. Phase ranges are calculated simply by multiplying the cycle count N by the wavelength, which is a known value for the L_1 and L_2 frequencies ($\lambda_L = \frac{c}{f_L}$). The differential phase range is then calculated as

$$\Delta L = -\left(N_{L1}\lambda_{L1} - N_{L2}\lambda_{L2}\right) \tag{2.4}$$

The TEC is then calculated in a fashion similar to equation (2.3):

$$TEC = \frac{\Delta L}{40.3} \frac{f_{L1}^2 f_{L2}^2}{f_{L1}^2 - f_{L2}^2} + b + B \tag{2.5}$$

where b is the phase ambiguity term.

In many contexts, it is important to employ techniques that compensate for the biases (B and b). When quantifying TEC *variation*, however, the TEC is typically either (1) filtered or (2) de-trended using a polynomial. In either case, only variations in the signal survive, and so the biases are no longer present. For TEC calculated in this study, phase range measurements were used.

The TEC calculated above is "slant" TEC (STEC), because the integration path involves a direct line-of-sight to the satellite. This can cause unwanted amplification of the TEC for low elevation angles due the longer integration path. In this study, STEC is converted to vertical TEC (VTEC) as the product of the STEC and $\cos(\alpha)$, with α defined as

$$\alpha = \arcsin\left(\frac{a}{a+h}\cos(\theta_e)\right) \tag{2.6}$$

where a is the radius of the earth (6371.2 km), h is the height of the thin ionospheric shell (here, taken as 350 km), and θ_e is the elevation angle of the receiver-satellite range vector. The thin ionospheric shell model assumes that

all of the TEC is contained within a thin shell at an altitude of h. Conversion to VTEC (in some sense) accounts for the elevation dependent enhancement that can occur.

2.1.1 Cycle Slips

An issue with using phase range measurements to calculate total electron content is the presence of cycle slips in the cycle count. Cycle slips are caused by a temporary loss of lock on the carrier by the GPS receiver. This causes a discontinuity in the TEC, which is interpreted as a high frequency spike in the frequency domain. This affects the filtering process and can lead to nonphysical frequencies appearing at the output of the filter. In some cases, too many cycle slips makes the data entirely unfilterable. Thus, it is important to compensate for cycle slips. In this study, a simple algorithm was designed to remove obvious cycle slips after the straightforward calculation of the TEC. First, all gaps in the data are closed by linearly interpolating between available points. Assuming that the sample rate of the TEC is T_s, let the length of the TEC data be N, where $TEC[0]$ represents the TEC at time t_0. Then, $TEC[i]$ is the value of the TEC at time $t_0 + iT_s$. Starting with $i = 1$, $j = 1$ we compute

$$\Delta TEC_j[i] = TEC_j[i] - TEC_j[i-1] \tag{2.7}$$

and check the threshold

$$Q(\Delta TEC_j[i]) = \begin{cases} \Delta TEC_j[i] & : x \geq \alpha \\ 0 & : x < \alpha \end{cases} \tag{2.8}$$

when $x \geq \alpha$, a cycle slip is considered to occur. Denote $Q(\Delta TEC_j[i])$ as Q_{ij}. A new signal TEC_{j+1} is constructed as

$$\begin{aligned} \{TEC_j[0] - Q_{ij},\, TEC_j[1] - Q_{ij},\, \cdots, TEC_j[i-1] - Q_{ij}, \\ TEC_j[i],\, TEC_j[i+1],\, \cdots, TEC_j[N-1]\} \end{aligned} \tag{2.9}$$

that shifts all of the previous $i - 1$ samples by $\Delta TEC_j[i]$ only if a cycle slip occurred. The algorithm then proceeds to the next value of i until reaching the $(N-1)$th sample, arriving at the final output signal $TEC_N[n]$. An

input-output comparison of the algorithm applied to a TEC signal is shown in Figure 2.1.

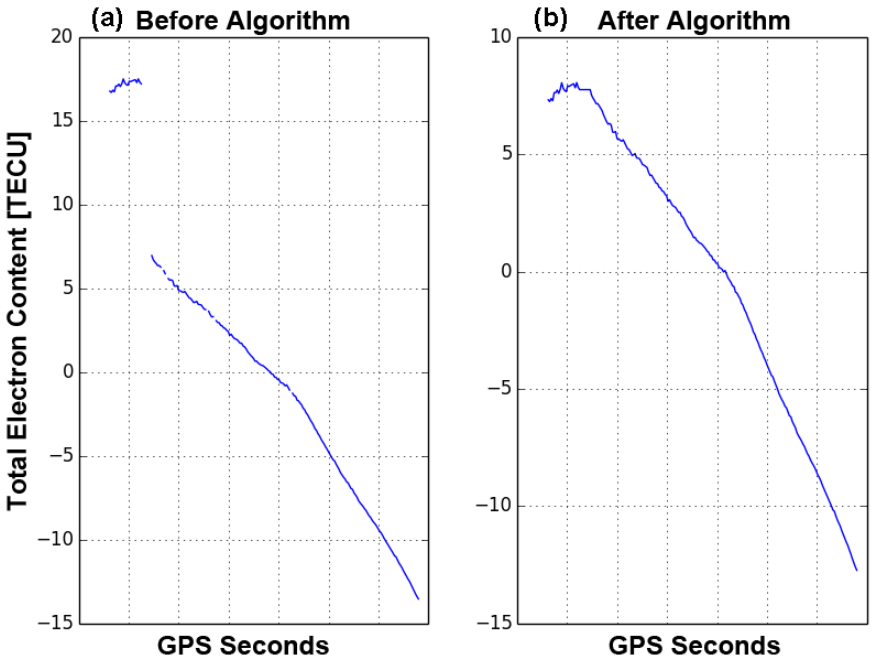

Figure 2.1: Application of the cycle slip removal algorithm to a TEC signal. Before (a) and after (b) plots are shown.

It should be noted that the algorithm does not preserve biases present in the signal. Applications that need the biases to remain intact require more advanced cycle slip removal techniques.

2.1.2 Filtering

In this study, we seek the *perturbation* in the total electron content that is induced by a tsunami. The perturbation is extracted by subjecting $TEC_N[n]$ to a length 50 FIR 1 mHz - 10 mHz bandpass filter. The frequency response and phase response of the filter are shown in Figure 2.2a and 2.2b, respectively. The filter coefficients (generated using the *firwin* function in SciPy, a numerical analysis package for Python) are shown in Table 2.1.

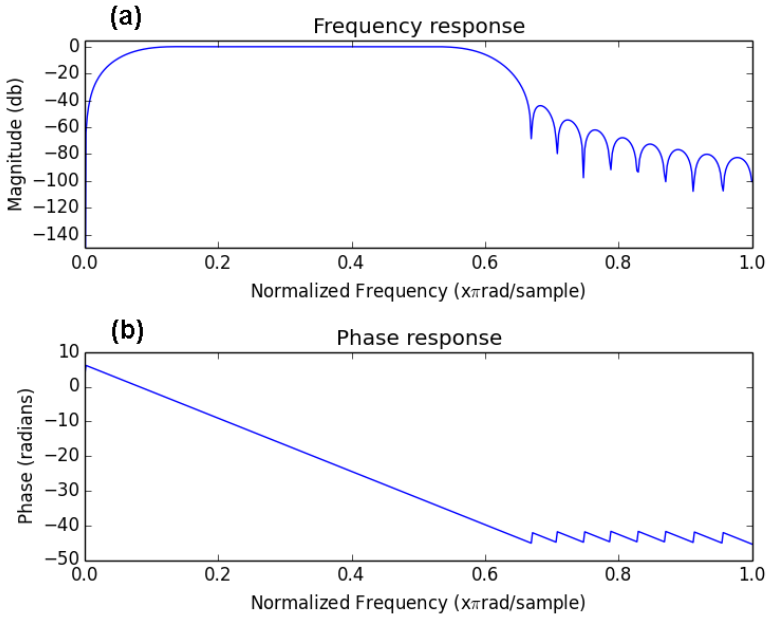

Figure 2.2: (a) Frequency response of the TEC filter. (b) Phase response of the TEC filter.

Table 2.1: Filter coefficients used to filter $TEC_N[n]$.

Start	**Stop**				
h[0]	h[3]	0	7.20920063e-05	-1.93704500e-05	6.06785356e-04
h[4]	h[7]	1.48766961e-03	-4.62819788e-04	9.52886434e-05	3.97511078e-03
h[8]	h[11]	-1.58560808e-03	-6.31561833e-03	3.14609435e-03	-2.66524866e-03
h[12]	h[15]	-2.12863290e-02	-8.21408371e-03	-2.49720691e-03	-4.08551379e-02
h[16]	h[19]	-3.66102270e-02	-5.23564500e-04	-5.22726579e-02	-8.63553406e-02
h[20]	h[23]	2.44679061e-03	-2.77716795e-02	-1.82012309e-01	4.64981502e-03
h[24]	h[27]	4.52967555e-01	4.52967555e-01	4.64981502e-03	-1.82012309e-01
h[28]	h[31]	-2.77716795e-02	2.44679061e-03	-8.63553406e-02	-5.22726579e-02
h[32]	h[35]	-5.23564500e-04	-3.66102270e-02	-4.08551379e-02	-2.49720691e-03
h[36]	h[39]	-8.21408371e-03	-2.12863290e-02	-2.66524866e-03	3.14609435e-03
h[40]	h[43]	-6.31561833e-03	-1.58560808e-03	3.97511078e-03	9.52886434e-05
h[44]	h[47]	-4.62819788e-04	1.48766961e-03	6.06785356e-04	-1.93704500e-05
h[48]	h[49]	7.20920063e-05	0		

The filter is applied in both the forward and backward direction (a zero phase filter) to generate the output signal $FTEC[n]$.

2.1.3 Receiver Networks

To properly study the characteristics of a gravity wave using total electron content, a spatial network of GPS receivers can be used to generate a collection of line-of-sight (LOS) TEC measurements for each visible satellite. The GPS network used in the study is shown in Figure 2.3a. If the ionosphere is viewed as a thin shell surrounding the earth at a height h (the same h and assumption made in Equation 2.6), each TEC signal can be taken as though it was measured at the intersection of the receiver-satellite range vector and the ionospheric shell. Then, for a given visible satellite, the receiver network will generate a grid of *ionospheric pierce points* (IPPs) that can be associated with a time varying TEC signal. The geometry of the grid is determined by the geometry of the receiver network and the location of the satellite. The position of the grid will move over time as its associated satellite enters and leaves the field of view of the receiver network. Several GPS satellites will always be in view, and so the GPS network will generate multiple *pierce point geometries*. A snapshot in time of a GPS network measuring filtered TEC simultaneously from five different pierce point geometries is shown in Figure 2.3(b).

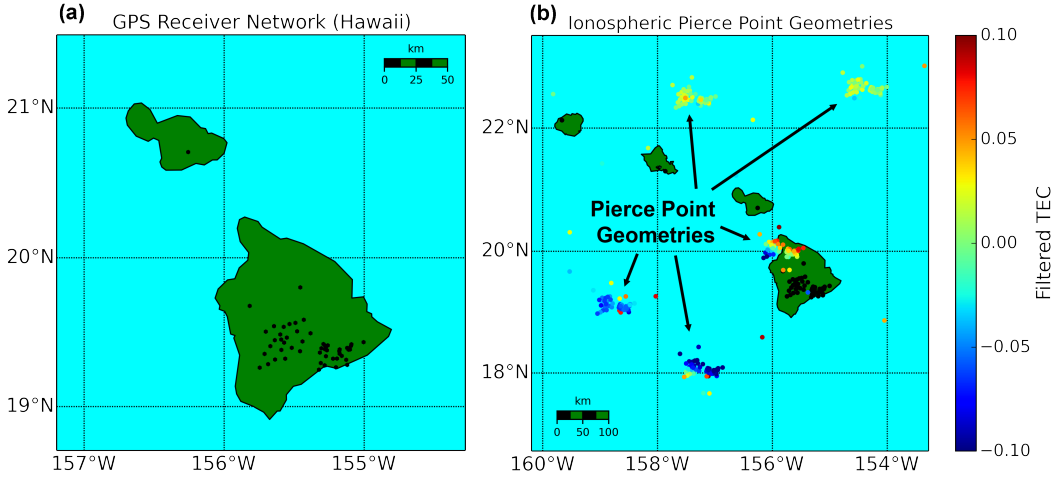

Figure 2.3: (a) The UNAVCO GPS network used in this study. (b) The GPS network and pierce point geometries measuring filtered total electron content from five different satellites.

The availability of dual-frequency receiver networks to generate grids of

ionospheric pierce points allows the use of a collection of techniques to calculate the properties of a gravity wave that has coupled into the ionosphere and produced a response in the TEC.

The phase speed and period of an internal gravity wave appearing in the TEC can be estimated using a hodochrone. A hodochrone is just a "distance to epicenter vs. time" plot. The slope of a line aligned with the maxima (or minima) for each receiver in the GPS network will be an estimate of phase speed, and the distance in time between the central value of two maxima (or minima) will be an estimate of the period. Knowing these two quantities allows the wavelength to be calculated as $\lambda = v_p T$. Examples of the technique are shown in Figure 2.4. The reported phase speed is the average slope of the slanted lines, and the reported period is the average time between the vertical lines.

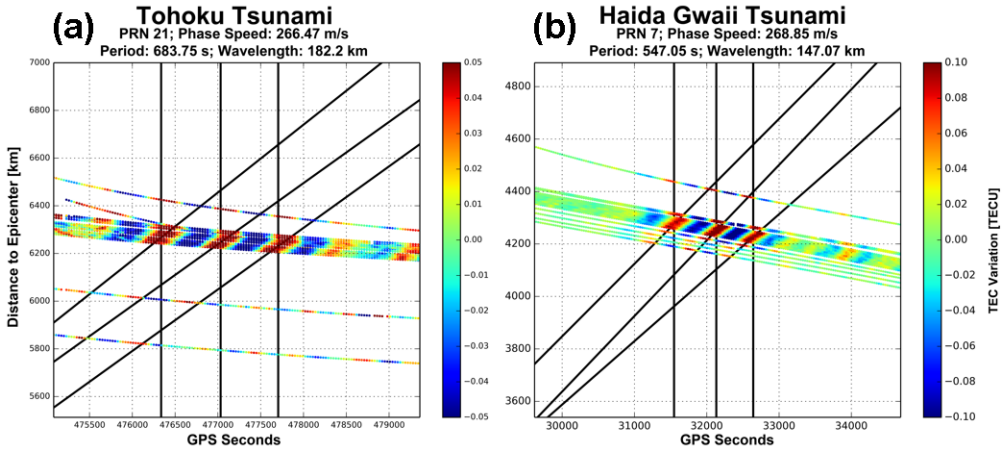

Figure 2.4: Hodochrones allow the estimation of the phase velocity and period of the tsunami signature. (a) A hodochrone showing the signature in the TEC from the March 2011 Tohoku tsunami. (b) A hodochrone for the TEC signature of the October 2012 Haida Gwaii tsunami.

The internal gravity wave phase velocity vector orientation can be estimated (azimuth and elevation) in the vicinity around a collection of ionospheric pierce points generated by a sufficiently dense GPS network. Azimuth is estimated using a geometric approach that calculates the local azimuth of a wavefront-orthogonal line placed over a pierce point geometry. Example results are shown in Figure 2.5. Barycentric interpolation was applied to the grid to create a continuous surface prior to calculation.

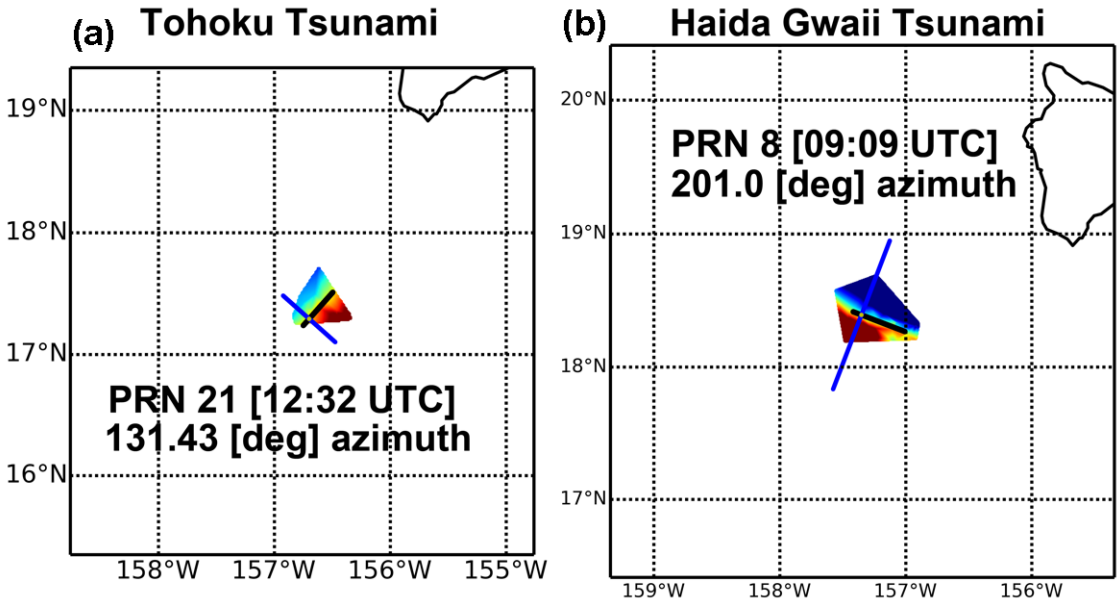

Figure 2.5: The azimuth of a wave in the TEC can be determined using a wavefront-orthogonal line. (a) Example result from the Tohoku event. (b) Example result from the Haida Gwaii event.

Estimates for the elevation, θ_G, of the internal gravity wave were determined by inferring the angular frequency, ω, and horizontal wavenumber, k_h, of the gravity wave from a hodochrone diagram using the methods above, and then utilizing the dispersion relation from *Occhipinti et al.* (2008):

$$k_v = \sqrt{\left(\frac{N^2-1}{\omega^2} - 1\right) k_h - \left(\frac{N^2}{2g}\right)^2} \tag{2.10}$$

where N is the Brunt-Väisälä frequency, g is gravitational acceleration, and k_v is the vertical wavenumber of the gravity wave. The elevation is then

$$\theta_G = -\tan^{-1}\left(\frac{k_v}{k_h}\right) \tag{2.11}$$

If a tsunami propagation model is available, comparing the tsunami travel time (TTT) to the time after earthquake (T) can reveal information about structures propagating with the tsunami in the signal. So called 'T-TTT' diagrams (the difference between the time after the earthquake and the tsunami travel time) can be created. This is useful if there is doubt cast on the origin of a signature in the TEC. Figure 2.6 shows an example T-TTT diagram.

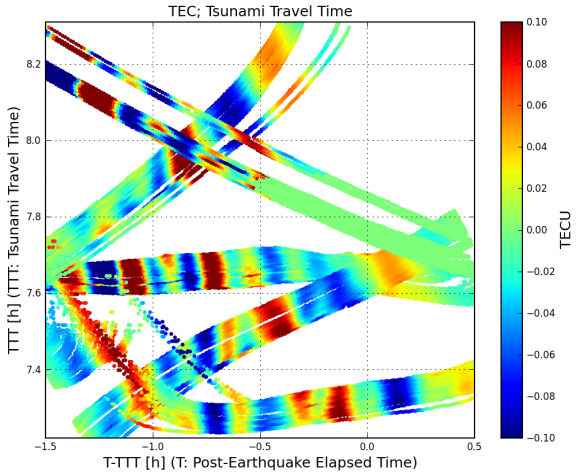

Figure 2.6: T-TTT vs. TTT for the 2011 Tohoku Tsunami observed from the UNAVCO GPS network.

A structure propagating in the TEC that is traveling in the same direction and the same speed as the tsunami will result in the structure having a constant value for T-TTT. Thus, vertical bands that appear in the diagram indicate structures that are traveling with the tsunami. If T-TTT is negative, the structure is *behind* the tsunami, and if it is positive, the structure is *ahead* of the tsunami.

2.2 Airglow Imaging Systems

Tsunami-generated gravity waves can also generate a signature in airglow emissions, which can be detected with an imaging system. In this study, two imaging systems located in Hawaii are utilized: The *Cornell Narrow Field Imager* and the *Cornell All Sky Imager* (CNFI and CASI), both of which are situated atop the Haleakalā volcano on the Hawaiian islands. The images produced by these systems can be used to measure wave parameters. Figure 2.7 shows the field of view for both cameras, along with an example image. In order to study the tsunami signature in the airglow layer, consecutive images are subtracted from one another in order to enhance any wave features present, as is commonly done in studies of mesospheric gravity waves (e.g., *Swenson and Mende*, 1994).

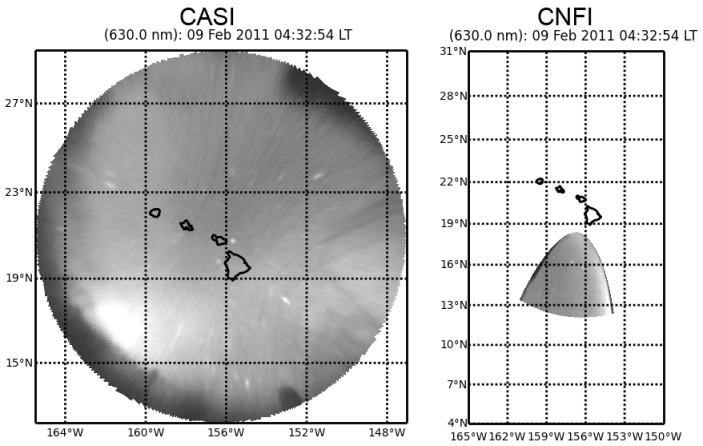

Figure 2.7: Field of view for the Cornell All Sky Imager and the Cornell Narrow Field Imager, situated atop the Haleakalā volcano on the Hawaiian islands.

Two methods can be used to estimate the orientation of a gravity wave that appears in an airglow image. The first method is analogous to the method used with GPS receiver networks, whereby the azimuth of a wavefront-orthogonal line is calculated. Figure 2.8 shows an example of the technique applied during the arrival of the 2012 Haida Gwaii tsunami to Hawaii. This method also produces an estimate of the wavelength, taken as the average distance between the yellow markers.

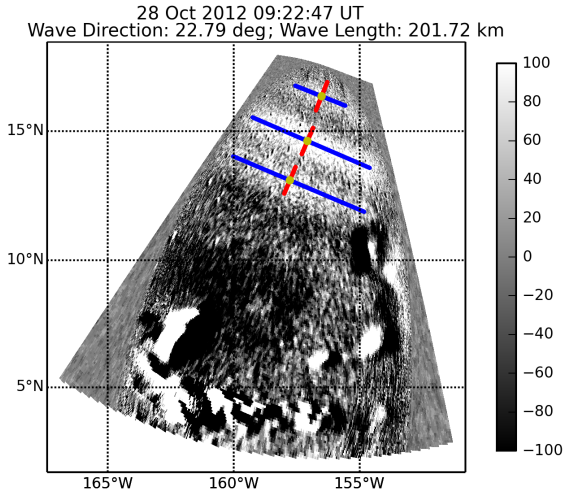

Figure 2.8: Example of the wavefront-orthogonal azimuth estimation method.

Another method applies a Gabor filter to the image and maximizes the output energy as a function the orientation of the Gabor kernel. The filter output for several different kernel orientations are shown in Figure 2.9.

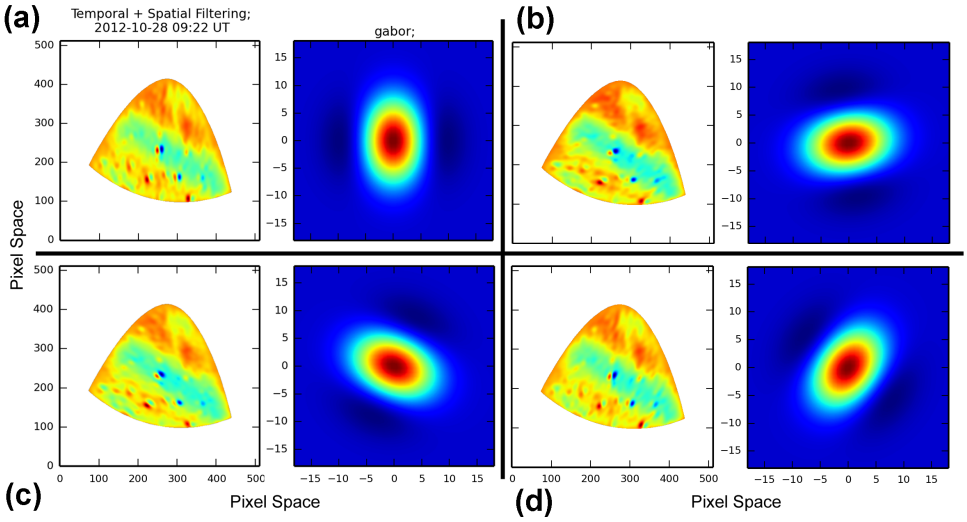

Figure 2.9: Filtered airglow image output using four different Gabor filter orientations (a,b,c,d). The result with the maximum image energy is an estimate of the wave orientation.

Figure 2.10 shows the dependence the image energy has on the rotation of the Gabor kernel. A kernel properly aligned with the wave in the airglow image will result in a filtered image that has more energy. The maxima of this curve can act as a measurement of the wave azimuth.

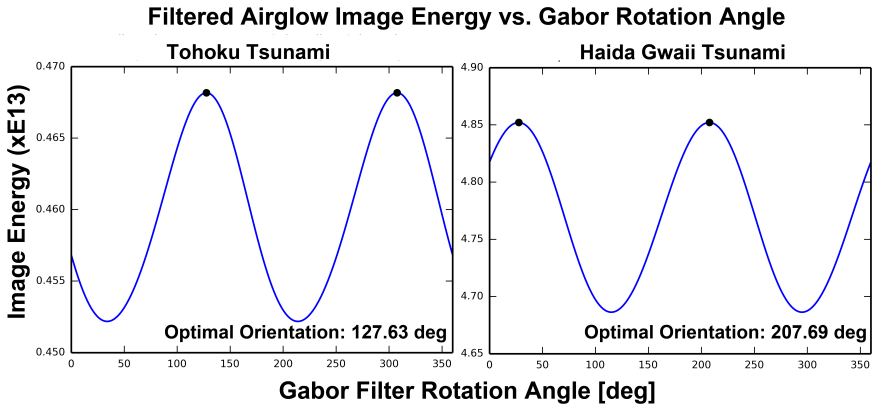

Figure 2.10: Gabor rotation angle vs. image energy. The maxima are taken as an azimuth measurement.

Wavelength can also be estimated by using pixel intensities along a profile orthogonal to the wavefront. The red line in Figure 2.11 is an example profile. Pixels around the red line are extracted and interpolation is applied over the pixels such that the output is collapsed to a one dimensional signal along the profile. The distance between the spatial coordinates between successive maxima provide an estimate of wavelength. The presence of multiple frequency waves in the signal can potentially skew the measurement, because not all local maxima may belong to the same frequency wave.

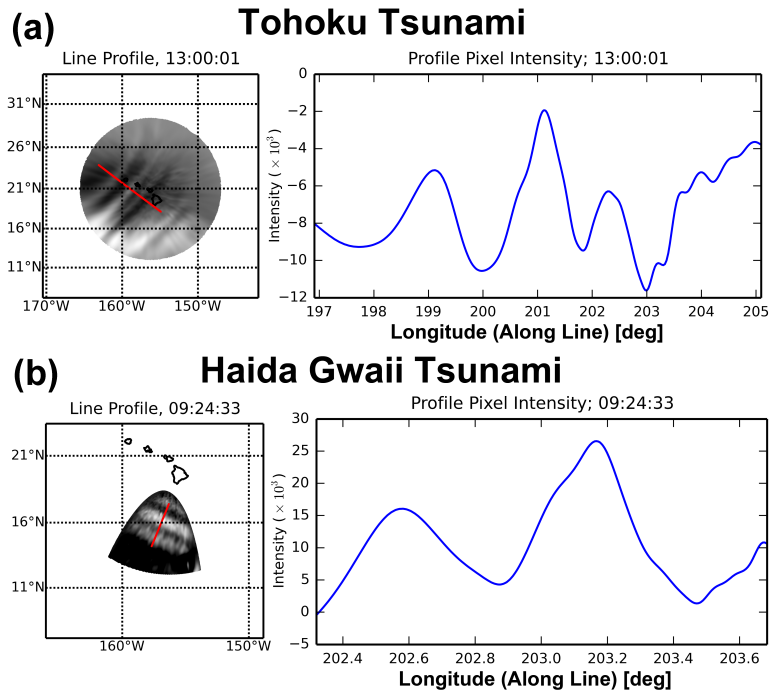

Figure 2.11: Examples of the pixel profile technique for estimating wavelength using an airglow imaging system. The distance between the coordinates of the two peaks of the wave is an estimate of wavelength. (a) and (b) show the technique applied to airglow images of the Tohoku and Haida Gwaii tsunamis signatures, respectively.

CHAPTER 3

COUPLING EFFICIENCY

Plasma motion in the ionosphere is in large part dictated by the orientation of the local geomagnetic field. The plasma response to a gravity wave that is propagating in the direction of the geomagnetic field feels less resistance than one propagating orthogonal to the field. Therefore, tsunami wave fronts propagating with large components in the direction of the local magnetic field will produce gravity waves more suitably aligned for ionospheric coupling, which can generate larger signatures in the TEC and the airglow emission. Furthermore, because the total electron content is an integrated line-of-sight measurement, the orientation between the receiver and satellite also plays a role in the coupling efficiency. Integration across phase fronts tends to cancel out variation. Therefore, integration paths that lie along phase fronts of the gravity wave tend to produce larger variations than paths that cross phase fronts. Thus, both the orientation of the tsunami with the local field and the observing geometry (i.e., the lines-of-sight from a ground-based GPS receiver and GPS satellite) will play a role in the observability of the ionospheric perturbation associated with the tsunami-generated gravity waves. The geometry of the problem is shown in Figure 3.1.

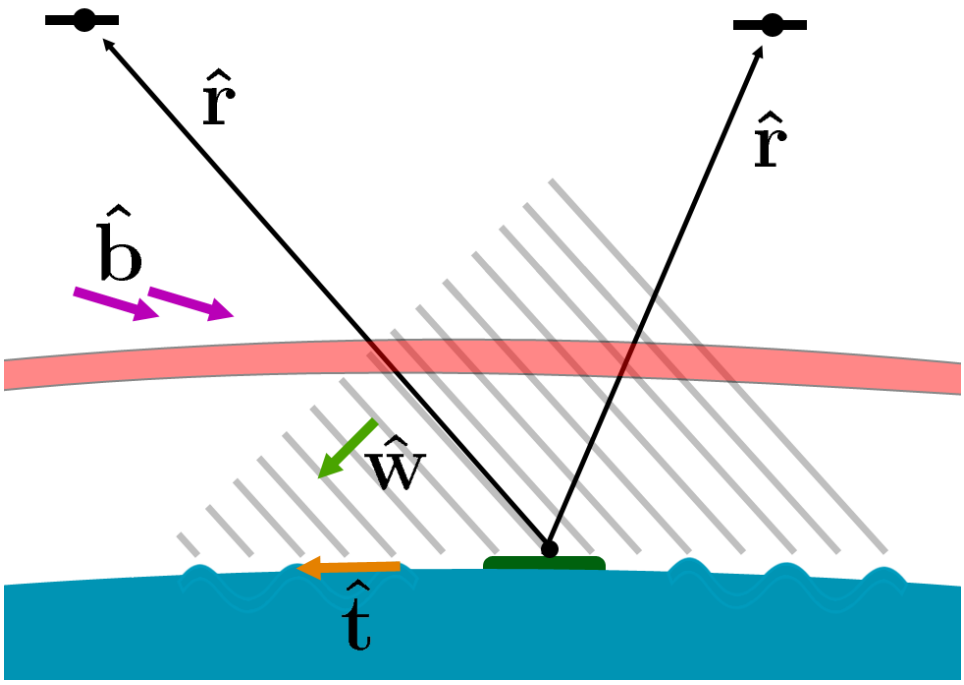

Figure 3.1: Various dependencies of the orientation factor. Line-of-sight paths that lie along lines of constant phase enhance the integration characteristic of the TEC measurement and lead to larger variation. Additionally, the angle between the magnetic field and the phase velocity of the gravity wave can enhance or attenutate the TEC variation.

To quantify the dependence of both the filtered VTEC and airglow measurements on the orientation between the gravity wave and the geomagnetic field as well as the observation geometry, we develop two orientation factors, o_1 and o_2, defined as

$$o_1 = |(\hat{\mathbf{w}} \times \hat{\mathbf{t}} \times \hat{\mathbf{w}}) \cdot \hat{\mathbf{b}}| \tag{3.1}$$

$$o_2 = |\hat{\mathbf{w}} \times \hat{\mathbf{r}}| \tag{3.2}$$

where $\hat{\mathbf{w}}$ is a unit vector in the direction of the gravity wave phase velocity, $\hat{\mathbf{t}}$ is a unit vector pointing in the tsunami propagation direction (with the same azimuth as $\hat{\mathbf{w}}$), $\hat{\mathbf{b}}$ is a unit vector in the direction of the local geomagnetic field at the same altitude as the grid of ionospheric pierce points (350 km in this study), and $\hat{\mathbf{r}}$ is the normalized receiver-satellite range vector. An estimate of the orientation of the local magnetic field can be obtained from the International Geomagnetic Reference Field (IRGF-11; *Finlay et al.*, 2010).

o_1 quantifies the amount of alignment between the gravity wave and Earth's magnetic field, and o_2 quantifies the amount of orthogonality between the gravity wave and the receiver-satellite range vector (or the elevation of a pixel, in the case of an airglow imaging system).

An overall observation factor can be obtained as the product of o_1 and o_2, which can be written as

$$|\sin(\beta)\left(b_x \sin(\phi_G)\sin(\theta_G) + b_y \cos(\phi_G)\sin(\theta_G) - b_z \cos(\theta_G)\right)| \tag{3.3}$$

with

$$\begin{aligned} \beta &= \arccos\left(\hat{\mathbf{w}} \cdot \hat{\mathbf{r}}\right) \\ \hat{\mathbf{w}} &= \begin{bmatrix} T\sin(\phi_G) \\ T\cos(\phi_G) \\ \sin(\theta_G) \end{bmatrix} \\ T &= \sqrt{w_x^2 + w_y^2} \end{aligned}$$

where b_x, b_y, b_z are the east, north, and up (ENU) components of a unit vector parallel to the local geomagnetic field, β is the angle between the receiver-satellite range vector $\hat{\mathbf{r}}$ and the phase velocity of the gravity wave, and θ_G, ϕ_G are the elevation and azimuth of the gravity wave phase velocity, respectively. When using a GPS network, $\hat{\mathbf{r}}$ is calculated by determining the position of each satellite relative to each receiver using publicly available GPS ephemeris information from the Crustal Dynamics Data Information System (available at ftp://cddis.gsfc.nasa.gov/gnss/data/daily/).

Notice that o_1 can be written as

$$o_1 = T\,|\sin(\theta_G)\cos(\phi_B - \phi_G) - \tan(\theta_B)\cos(\theta_G)| \tag{3.4}$$

where ϕ_B and θ_B are the azimuth and elevation of the local geomagnetic field in the same ENU coordinate system described above. It is straightforward to show that Equation 3.4 maximizes ($o_1 = 1$) when $\phi_G = \phi_B$ and $\theta_G = \theta_B \pm \pi/2$. This is the case when the phase fronts of the gravity wave are in perfect alignment with magnetic field and the induced motion is along the magnetic field line in which a high coupling efficiency would indeed be expected. Additionally, $o_2 = \sin(\beta)$ maximizes when $\hat{\mathbf{w}}$ and $\hat{\mathbf{r}}$ are orthogo-

nal; this is analogous to the case when $\hat{\mathbf{r}}$ also lies in direct alignment with the phase fronts of the gravity wave, representing the case when the TEC integration path is along constant phase.

Limitations of the orientation factor include the plane wave assumption, and the spatial scale of the measurement network used. Firstly, internal gravity waves are not expected to be globally planar; they instead have a characteristic "upturning", briefly mentioned in *Hooke* (1968) and shown in the results of *Occhipinti et al.* (2006). Since the TEC measurement is a path integration, it is not associated with a particular point in space. Changes in the elevation of the gravity wave occur along the integration path, a geometric feature that is not captured by the orientation factor. Secondly, when calculating a single orientation factor surface representative of a receiver network, the receivers themselves should be close enough to each other such that the individual receiver-satellite range vectors ($\hat{\mathbf{r}}$) are sufficiently approximated using a single average vector representative of the entire network. The average vector approximation was used in this study, but would not be acceptable in the case of larger networks such as GEONET. In those cases, multiple surfaces would need to be calculated for different locations throughout the network. However, this concern goes away when using data from a single location, such as provided by an imaging system.

CHAPTER 4

CASE STUDIES

The tsunami resulting from the 2011 Tohoku 9.0 Mw earthquake produced a clear wave signature in the upper atmosphere, which was observed both using the 630.0-nm airglow emission and measurements of the TEC. In 2012, another earthquake (Mw 7.8, Haida Gwaii) resulted in a tsunami that also yielded a signature in the ionosphere. These are the only two known measurements of the tsunami-induced signature in the airglow layers ever made and provide an important dataset to understanding ocean-atmosphere coupling processes.

4.1 28 October 2012 Haida Gwaii Tsunami

At 03:04 UT on 28 October 2012 an earthquake (Mw 7.8) occurred in the Haida Gwaii region along the western coast of Canada. According to the U.S. Geological Survey (USGS) (data available from http://earthquake.usgs.gov/) the epicenter was located at 52.742°N, 132.131°W (± 12.2 km) and was 20.1 km (± 2.7 km) below the surface. The earthquake subsequently generated a tsunami that propagated throughout the Pacific Ocean, resulting in sea surface variations not exceeding 10 cm in the open ocean between Hawaii and the epicenter as shown in *Lay et al.* (2013). The arrival of the tsunami to DART station 51407 close to Hawaii occurred between 08:30 and 09:00 UT, with sea surface variations not exceeding 2 cm. A snapshot of the ionospheric pierce points at 09:06 UT along with a hodochrone are shown in Figure 4.1.

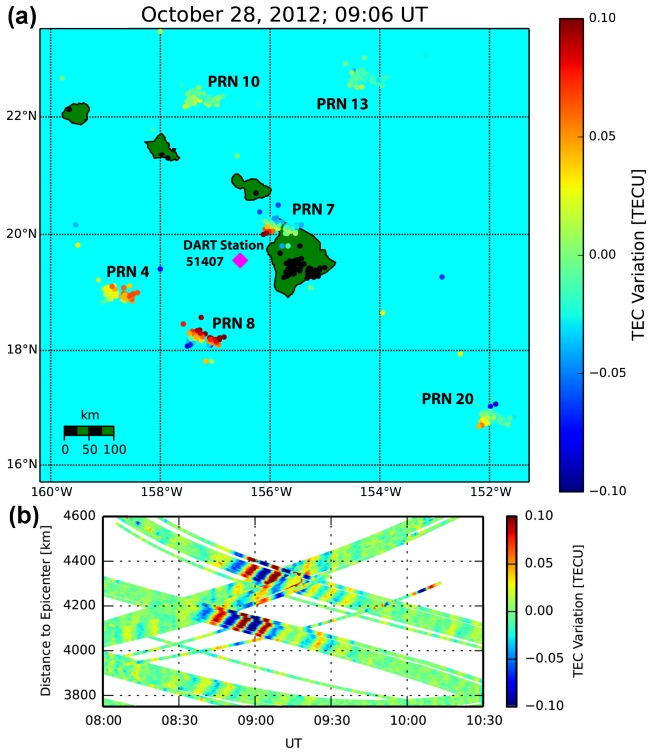

Figure 4.1: (a) Observation geometry, showing ionospheric pierce points with superimposed filtered TEC during 9:06 UT. The magenta diamond is the location of DART station 51407. The black points over the islands show the dual-frequency GPS receiver network used in this study. (b) Hodochrone generated from satellite ephemeris information with TEC variation superimposed as color. The ionospheric signature is strong in the TEC between 8:30 and 9:30 UT.

Observations made using the techniques of Chapter 2 indicate the presence of an ionospheric signature over Hawaii associated with the passage of the 2012 Haida Gwaii tsunami. Figure 4.2 compares the filtered TEC derived from GPS satellite PRN 8 from all available receivers to the sea surface variation reported by DART station 51407 during the passing of the tsunami in Hawaii. The receiver sites are listed in descending order with respect to latitude. At about the same time as the tsunami arrival, a strong signal appears in the filtered TEC above Hawaii (Figure 4.2a) with amplitudes reaching 0.15 TECU. The DART station was approximately 213 km away from the mean position of the PRN 8 pierce points at the onset of the TEC perturbation. The tidal gauge data (Figure 4.2b) indicate very small perturbations (less than 2 cm) on the ocean surface. However, the perturbations on the ocean

and in the ionosphere have similar periods (the tidal gauge shows a period of nearly 10 minutes between the first two tsunami crests, indeed falling within the 8.7 to 14 minute periods we observed in the ionosphere) and the orientation seen in the ionospheric perturbations (Figures 4.1 and 4.3) indicate that these perturbations are related to this small-amplitude tsunami when compared to the tsunami model shown by *Lay et al.* (2013).

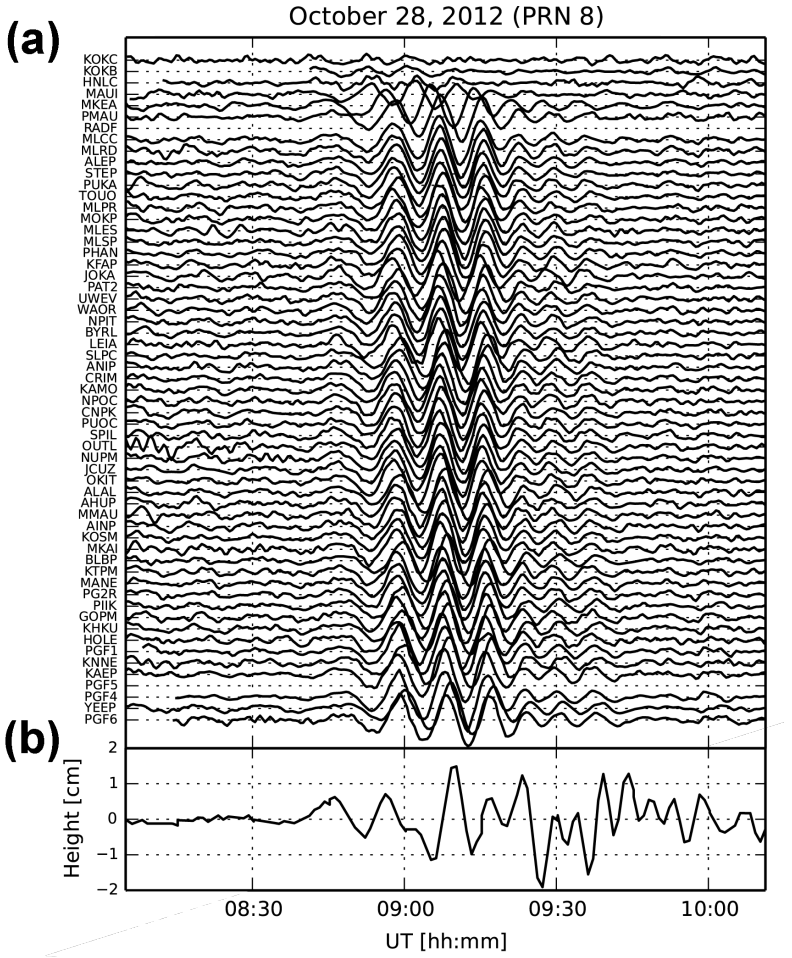

Figure 4.2: Comparison of the filtered TEC for PRN 8 (a) and de-trended tidal gauges (b) suggest the tsunami as the origin of the perturbation. Plots of filtered TEC for the other visible satellites have similar structure.

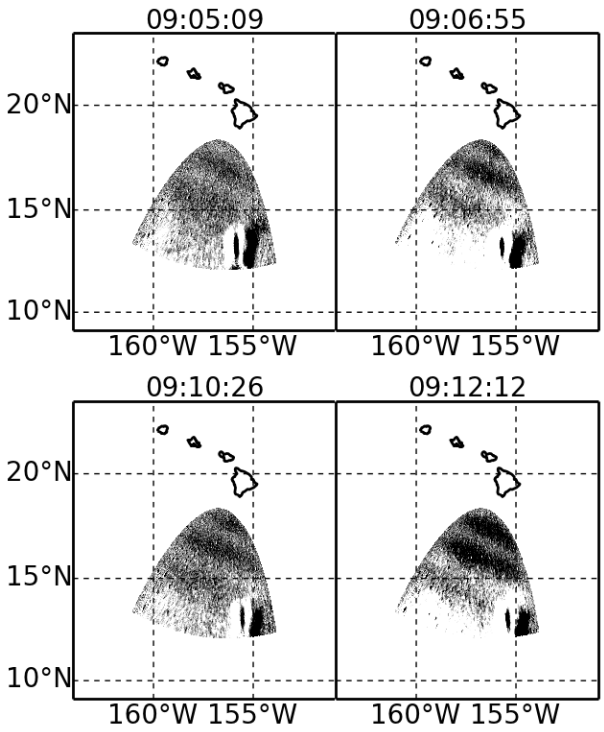

Figure 4.3: The coupling was seen in differenced airglow images of the 630 nm emission following the signature in the TEC. This is the second observation ever of a tsunami producing a signature in the airglow, after *Makela et al.* (2011) revealed similar coupling effects in the airlow caused by the 2011 Tohoku event. The four airglow successive airglow images shown show clear wave structures similar to those seen in the TEC.

Using the techniques developed in Chapter 2, the parameters of the generated gravity wave are presented in Table 4.1.

Table 4.1: Estimated gravity wave parameters (near Hawaii) for the 28 October, 2012 Haida Gwaii Tsunami inferred from the ionospheric signal.

Estimated Parameter	**Min**	**Max**
Phase Speed	219 m/s	340 m/s
Period	8.7 min	14 min
Wavelength	115 km	254 km
Azimuth Angle	200 deg	207 deg
Elevation Angle	-33 deg	-57 deg

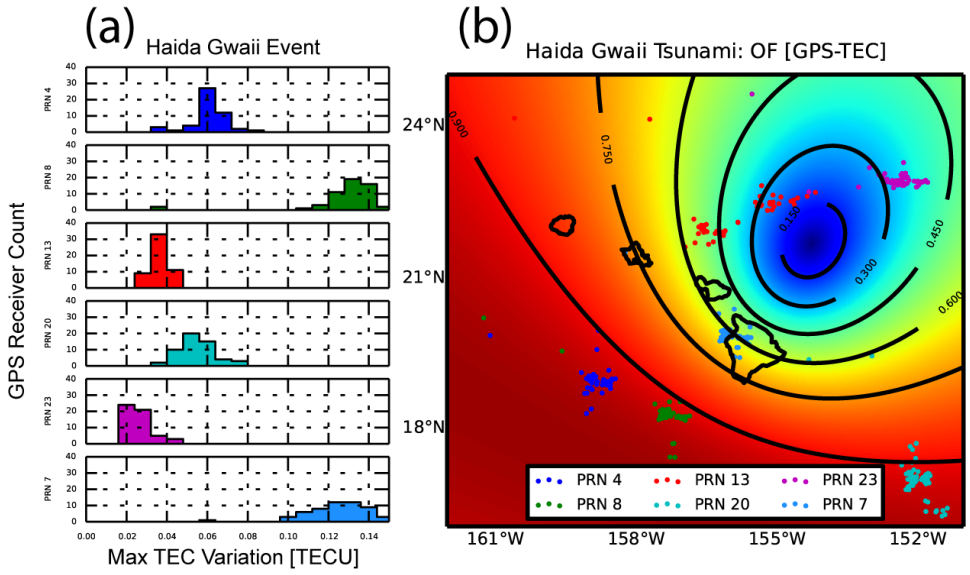

Figure 4.4: (a) The distribution of maximum tsunami-generated wave amplitudes observed in the TEC. (b) Calculated OF using an input plane wave similarly oriented to the wave observed in the filtered TEC for the Haida Gwaii event. The calculation reveals that locations on the opposite side of the islands relative to the tsunami arrival direction have higher observability.

A closer examination of the TEC data indicate that observations made from the Hawaiian islands to different GPS satellites exhibit different perturbation amplitudes. This is shown in Figure 4.4a, where histograms of the TEC perturbations for all observations toward a given GPS satellite are presented. The histograms were generated by binning the *maximum* observed filtered TEC perturbations during the passage of the tsunami from each of the receiver sites for each satellite. The exact location of the pierce point during the maximum for each receiver site is then marked on the adjacent observation factor map (Figure 4.4b). For most satellites this results in a fairly localized set of points, the only exception being PRN 13 with two distinct locations where maxima occur depending on the location of the receiver.

Considerable anisotropy is present in the measurement of tsunami-generated TEC wave amplitudes; in the Haida Gwaii case, the tsunami signature was enhanced for satellites whose pierce points were to the southwest of Hawaii (e.g., PRN 4, 8), while measurements made to the northeast showed relatively smaller perturbations (e.g., PRN 13 and 23) towards satellites with relatively similar elevation angles. To understand this, we plot the observing

factor generated by utilizing the parameters inferred for this event (specified in Table 4.1) along with Equation 3.3. This is plotted as the colored surface in Figure 4.4b for the Haida Gwaii event. The largest observing factors are seen to the southwest of Hawaii, while the observing factor is significantly reduced to the northeast. The spatial variations shown in the surfaces of Figure 4.4 are mainly due to the effect of observation geometry; o_2 varies significantly based on whether the satellite is to the southwest or northeast of the main island. o_1 is nearly spatially constant over the region shown; this is due to the fact that the geomagnetic field is also nearly spatially constant at this scale.

4.2 11 March 2011 Tohoku Tsunami

A Mw 9.0 megathrust earthquake occured at 05:46 UT near the coast of Honshu, Japan with an epicenter located at (38.322° N, 142.369° E) and a depth of 30 km as reported by USGS. The earthquake generated a powerful tsunami with sea surface variations exceeding 20 cm at DART station 51407 (the same tidal gauge used in the Haida Gwaii marked in Figure 4.1), reaching Hawaii just before 13 UT. A hodochrone of the detected signature is shown in Figure 4.5 and our measured wave parameters are given in Table 4.2.

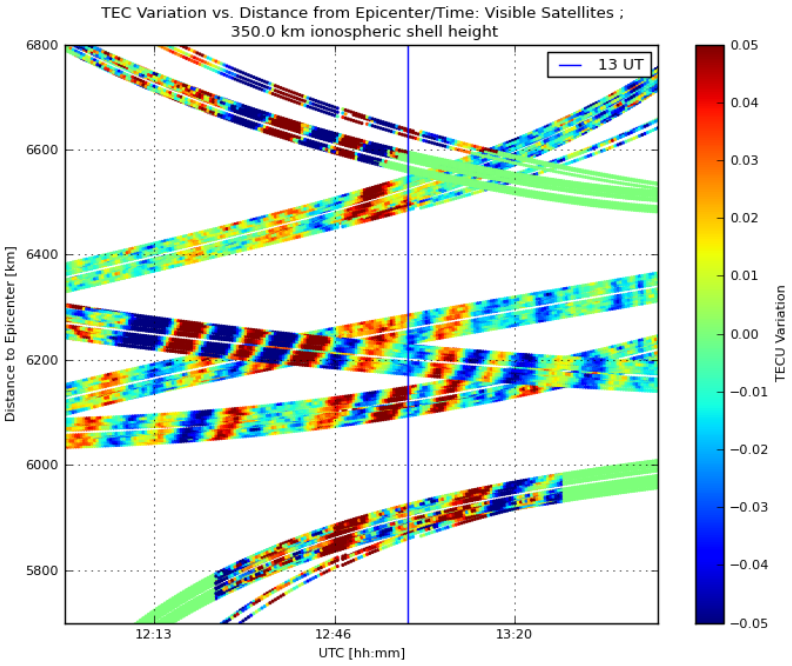

Figure 4.5: Hodochrone showing the ionospheric signature of the 11 March 2011 Tohoku tsunami calculated for a GPS receiver network on Hawaii.

Table 4.2: Measured wave parameters: Tohoku event

Estimated Parameter	**Min**	**Max**
Phase Speed	241 m/s	349 m/s
Period	10.1 min	14 min
Wavelength	157 km	273 km
Azimuth Angle	105 deg	131.9 deg
Elevation Angle	−44 deg	−56 deg

Histograms of the maximum TEC perturbations seen to four different GPS satellites are presented in Figure 4.6a, while the IPP locations and observing factor are shown in Figure 4.6b. As with the analysis of the Haida Gwaii event, there is a general relationship between the magnitude of the TEC perturbations and the observing factors at the IPPs. However, we do notice

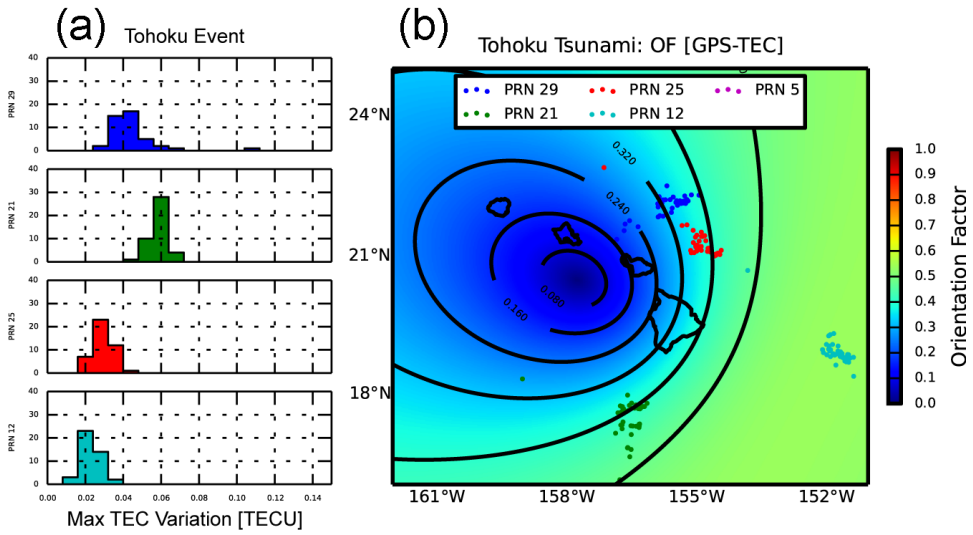

Figure 4.6: (a) The distribution of maximum tsunami-generated wave amplitudes observed in the TEC. (b) Calculated OF using an input plane wave similarly oriented to the wave observed in the filtered TEC for the Tohoku event.

that the perturbations to PRN 12, whose IPPs lie within a region of relatively high observing factor, are smaller than the observing factor seems to indicate.

4.3 Comparisons

The comparison of observing factors for these two events offer a potential explanation as to why the Haida Gwaii observations exhibit larger TEC fluctuation than seen in the Tohoku event, despite the fact that the underlying tsunami had smaller amplitudes for the Haida Gwaii example (less than 2 cm) than for the Tohoku example (greater than 20 cm). In the case of the Tohoku tsunami, the strong sea level variations generated an ionospheric signature in the TEC not exceeding 0.08 TECU. However, the weaker Haida Gwaii tsunami generated variations of up to 0.15 TECU. This can be understood through the orientation factor, which takes into account the alignment of the gravity wave with the geomagnetic field. In the case of the Haida Gwaii event, the arrival of the tsunami from the northeast generated gravity waves with azimuth angles (ϕ_G) close to the local magnetic field values (10° - 18° difference), a necessary condition for the maximization of o_1 (Equation 3.4) discussed in Chapter 3. Conversely, the arrival of the Tohoku tsunami from

the northwest (see, for example, *Makela et al.*, 2011), was closer to being orthogonal to the magnetic field (58° - 85° difference). These effects are clearly seen in Figure 4.4 and Figure 4.6, in which the orientation factor for the Haida Gwaii event maximizes near 1.0 to the southwest, while the maximum value in the Tohoku example is approximately 0.5.

Modeling results support the conclusions made about the effects observation geometry from the orientation factor. Figure 4.7 shows the Haida Gwaii image on top of a modeled airglow signal for the Haida Gwaii event. Notice the relative enhancement in the model values opposite the islands is collocated with the region corresponding to a nearly maximum orientation factor (Figure 4.4). The event was modeled by utilizing a gravity wave normal mode summation provided by IPGP (Institut de Physique du Globe de Paris) as an input to the Neutral Plasma Airglow Coupling model (NPAC) developed by P. Coïsson at the University of Illinois.

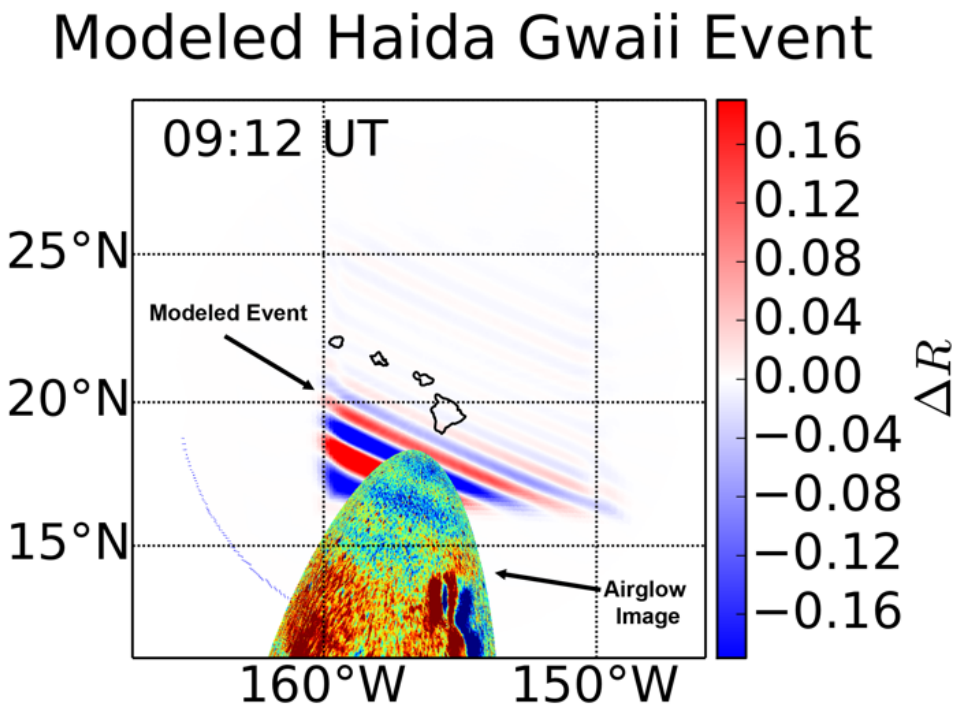

Figure 4.7: Results of a model are compared to an actual airglow image of the Haida Gwaii tsunami signature. The enhancement to the south west of the islands supports the observability prediction of the orientation factor.

CHAPTER 5

DISCUSSION AND CONCLUSIONS

In this work, we have shown the viability of dual-frequency GPS receiver networks and airglow imaging systems as tools for tsunami detection and analysis. We have developed an orientation factor which can be used to study the coupling efficiency between tsunami-generated gravity waves and the ionosphere. Using ionospheric perturbation data derived from a network of GPS receivers and an airglow imaging system, we have shown that this concept has utility in being able to quantitatively understand the relationship between observations of the earth's ionosphere and the underlying perturbations on the ocean. Surfaces of orientation factor (Figure 4.4b, Figure 4.6b) can be calculated "on-the-fly" without the need of extensive simulation, but at the expense of simplicity. Only a prediction of the gravity wave azimuth, elevation, and local magnetic field direction are required to compute orientation factor for a given receiver-satellite pair or airglow pixel. This makes it a potential future tool in a tsunami warning system, where deeper properties of the gravity wave are not known immediately after an earthquake.

The 0.15 TECU signatures show that the Haida Gwaii tsunami produced comparatively larger variations than the Tohoku event (0.15 vs. 0.08 TECU), despite the much weaker sea level variation (< 2 vs. > 20 cm). Through the development and application of the orientation factor, the close alignment of the tsunami propagation direction to the geomagnetic field is shown to likely be responsible for this. The orientation factor concept developed here offers a simple explanation to the anisotropy, ultimately suggesting that tsunami propagation along the geomagnetic field is more easily detected in the Earth's ionosphere. A strong disparity can exist between the sea level variations and the associated ionospheric perturbations when tsunami orientation and the observation geometry are not considered. This has significant implications for any tsunami monitoring tool that would rely on ionospheric observations to quantitatively infer ocean-level parameters.

CHAPTER 6

REFERENCES

Artru, J., V. Ducic, H. Kanamori, P. Lognonn, and M. Murakami (2005), Ionospheric detection of gravity waves induced by tsunamis, Geophys. J. Int., 160(3), 840-848, doi:10.1111/j.1365-246X.2005.02552.x.

Finlay, C.C., Maus, S., Beggan, C. D., Bondar, T. N., Chambodut A., Chernova, T. A., Chulliat A., Golovkov, V. P., Hamilton, B., Hamoudi M., Holme, R., Hulot G., Kuang, W., Langlais, B., Lesur, V. , Lowes, F. J., Lühr, H., Macmillan, S., Mandea, M., McLean, S., Manoj, C., Menvielle, M., Michaelis, I., Olsen, N., Rauberg, J., Rother, M., Sabaka, T. J., Tangborn, A., Tøffner-Clausen, L., Thébault, E., Thomson, A.W.P., Wardinski, I., Wei, Z., and Zvereva, T.I. (2010), International Geomagnetic Reference Field: The eleventh generation, Geophys. J. Int., 183, 1216-1230, doi:10.1111/j.1365-246X.2010.04804.x.

Hickey, M. P., G. Schubert, and R. L. Walterscheid (2010), Atmospheric airglow fluctuations due to a tsunami-driven gravity wave disturbance, J. Geophys. Res., 115, A06308, doi:10.1029/2009JA014977.

Hines, C. O. (1960), Internal atmospheric gravity Waves at ionospheric heights, Can. J. Phys., 38(11), 1441-1481, doi:10.1139/p60-150.

Hooke, W. H. (1968), Ionospheric irregularities produced by internal atmospheric gravity waves, (1966), J. Atmos. Terr. Phys, 30, 795-823, doi:10.1016/S0021-9169(68)80033-9.

Lay, T., L. Ye, H. Kanamori, Y. Yamazaki, K. F. Cheung, K. Kwong, and K. D. Koper (2013), The October 28, 2012 Mw 7.8 Haida Gwaii underthrusting earthquake and tsunami: Slip partitioning along the Queen Charlotte Fault transpressional plate boundary, Earth Planet. Sci. Lett., 375, 57-70, doi:10.1016/j.epsl.2013.05.005.

Liu, J. Y., Y. B. Tsai, S. W. Chen, C. P. Lee, Y. C. Chen, H. Y. Yen, W. Y. Chang, and C. Liu (2006a), Giant ionospheric disturbances excited by the M9.3 Sumatra earthquake of 26 December 2004, Geophys. Res. Lett., 33(2), L02103, doi:10.1029/2005GL023963.

Liu, J.-Y., Y.-B. Tsai, K.-F. Ma, Y.-I. Chen, H.-F. Tsai, C.-H. Lin, M. Kamogawa, and C.-P. Lee (2006b), Ionospheric GPS total electron content (TEC) disturbances triggered by the 26 December 2004 Indian Ocean tsunami, J. Geophys. Res., 111(A5), A05303, doi:10.1029/2005JA011200.

Lognonné, P., J. Artru, R. Garcia, F. Crespon, V. Ducic, E. Jeansou, G. Occhipinti, J. Helbert, G. Moreaux, and P.-E. Godet (2006), Ground-based GPS imaging of ionospheric post-seismic signal, Planet. Space Sci., 54(5), 528-540, doi:10.1016/j.pss.2005.10.021.

Makela, J. J., Midlatitude ionospheric studies using the global positioning system and airglow cameras Ph.D. dissertation, School of Electrical Engineering, Cornell University, Ithaca, New York, 2003.

Makela, J. J., Lognonné, P., Hébert, H., Gehrels, T., Rolland, L., Allgeyer, S., Kherani, A., Occhipinti, G., Astafyeva, E., Coïsson, P., Loevenbruck, A., E. Clévédé, Kelley, M. C., and Lamouroux, J. (2011), Imaging and modeling the ionospheric airglow response over Hawaii to the tsunami generated by the Tohoku earthquake of 11 March 2011, Geophys. Res. Lett., 38(13), doi:10.1029/2011GL047860.

Occhipinti, G., P. Lognonné, E. A. Kherani, and H. Hébert (2006), Three-dimensional waveform modeling of ionospheric signature induced by the 2004 Sumatra tsunami, Geophys. Res. Lett., 33(20), L20104, doi:10.1029/2006GL026865.

Occhipinti, G., E. A. Kherani, and P. Lognonné (2008b), Geomagnetic dependence of ionospheric disturbances induced by tsunamigenic internal gravity waves, Geophys. J. Int., 173(3), 753-765, doi:10.1111/j.1365-246X.2008.03760.x.

Occhipinti, G., L. Rolland, P. Lognonné, and S. Watada (2013), From Sumatra 2004 to Tohoku-Oki 2011: The systematic GPS detection of the ionospheric signature induced by tsunamigenic earthquakes, J. Geophys. Res. Sp. Phys., 118(6), 3626-3636, doi:10.1002/jgra.50322.

Peltier, W.R., and Hines, C.O. (1976), On the possible detection of tsunamis by a monitoring of the ionosphere, J. Geophys. Res., 81(12), 1995-2000.

Rolland, L. M., G. Occhipinti, P. Lognonné, and A. Loevenbruck (2010), Ionospheric gravity waves detected offshore Hawaii after tsunamis, Geophys. Res. Lett., 37(17), doi:10.1029/2010GL044479.

Swenson, G. R., and S. B. Mende (1994), OH emission and gravity waves (including a breaking wave) in allsky imagery from Bear Lake, UT, Geophys. Res. Lett., 21(20), 2239, doi:10.1029/94GL02112.